



Modeling the work hardening behavior in metastable high entropy alloys

Ravi Sankar Haridas ^{a,b,c}, Priyanshi Agrawal ^{a,b,c}, Rajiv S. Mishra ^{a,b,c,*}

^a Department of Materials Science and Engineering, University of North Texas, Denton, TX, 76207, USA

^b Center for Friction Stir Processing, University of North Texas, Denton, TX, 76207, USA

^c Advanced Materials and Manufacturing Processes Institute, University of North Texas, Denton, TX, 76207, USA



ARTICLE INFO

Keywords:

Martensitic transformation
High entropy alloys
Stacking fault energy
Plasticity
Work hardening

ABSTRACT

Mechanical response of transformation-induced plasticity (TRIP)-enabled metastable high entropy alloys that display austenite (γ) to martensitic (ϵ) phase transformation under uniaxial tension is characterized by a constant work hardening segment preceded and succeeded by stages of gradual drop in work hardening. A four-parameter empirical model based on the nature of the work hardening curve is developed. The model enjoys ease of parametric identification from macroscopic mechanical response over physically-based models. Compared to tensile deformation of conventional alloys, some insights are drawn from the numerical value of the model parameters for TRIP HEAs when fitted to their tensile deformation response. Further, a method to predict the tensile mechanical response of TRIP HEAs/steels based on the trends of correlated parameters with stacking fault energy and microstructure is proposed.

1. Introduction

The prospect of creating a solid solution in a multicomponent alloy system having five or more principal elements with no secondary or/and intermetallic phases by virtue of high entropy of mixing resulted in the development of a new class of alloys called high-entropy alloys (HEAs) [1]. Materials scientists were fascinated by the multi-principal elemental composition that facilitated HEAs to achieve a combination of high strength/hardness, ductility, corrosion resistance, wear resistance, high temperature properties, fatigue strength, and oxidation resistance [2]. The recent introduction of transformation induced plasticity (TRIP) in HEAs resulted in excellent strength-work hardening-ductility synergy as a result of solid solution hardening and phase metastability-driven work hardening [3–8]. ϵ -martensitic transformation is a strain-accommodating mechanism when loaded by an external force. Transformation of austenite to ϵ -martensite generally occurs if the stacking fault energy (SFE) is typically below 18 mJ/m^2 [9]. Deformation of TRIP HEAs/steels is characterized by the formation of planar defects such as stacking faults; stacking faults in f.c.c. generally form by the formation of $\frac{1}{6}\langle 112 \rangle\{111\}$ Shockley partials by dissociation of $\frac{1}{2}\langle 110 \rangle\{111\}$ dislocations. Earlier studies have confirmed that ϵ -martensite embryo forms when intrinsic stacking faults form on every other {111} plane in the f.c.c. austenite [10]. Mishra et al. [11], in their recent review, have given a detailed description of various aspects of

metastable TRIP HEAs from alloy design-processing-structure-property to deformation mechanisms in the transformed martensitic phase.

Several microstructure-based phenomenological models were proposed in the past to relate the contribution of microstructural features such as dislocation density, stacking fault energy, and nucleation rate of martensitic embryo to strength of TRIP steels [12–17]. However, the need for rigorous experiments and the identification of numerous model parameters limit their usage. To overcome such difficulties, empirical constitutive relations with minimal model parameters are preferred and are often used in finite element packages. Recently, Lloyd et al. [18] developed a work hardening-based empirical model for TRIP and TWIP steels, for which the work hardening curve is characterized by prolonged constant work hardening after the yield, followed by a sharp drop in work hardening and subsequent necking and failure. However, they neglected to take into account the initial drop in the work hardening rate during early deformation, which is typical of all metallic alloys including TRIP and TWIP steels. We propose a four-parameter hardening model for TRIP/TWIP HEAs based on the true nature of the hardening curve, which can also be extended to TRIP/TWIP steels. Although the model is not based physically on any microstructural mechanisms, an attempt is made to correlate the model parameters with the microstructure and stacking fault energy (SFE).

* Corresponding author. Department of Materials Science and Engineering, University of North Texas, Denton, TX, 76207, USA.

E-mail address: Rajiv.Mishra@unt.edu (R.S. Mishra).

2. Experimental methods

$\text{Fe}_{38.5}\text{Mn}_{20}\text{Co}_{20}\text{Cr}_{15}\text{Si}_5\text{Cu}_{1.5}$ metastable TRIP HEA (Cu-HEA) was utilized for the experimental study. Table 1 gives the nominal and actual compositions of the alloy produced via vacuum arc melting and subsequent casting. The cast material was warm rolled to quarter inch thickness and subsequently homogenized at 1100 °C for 1 h. ASTM E8 standard tensile samples were milled out from the homogenized Cu-HEA plate. Uniaxial tensile tests were performed on MTS 322 load frame at an initial strain rate of 10^{-3} s^{-1} . Samples for electron back scatter diffraction (EBSD) analysis were polished to 0.02 μm surface finish using colloidal silica. Microstructural characterization using EBSD was performed in a FEI Nova Nano SEM 230 equipped with a Hikari Super EBSD detector functioning at an operating voltage of 20 kV. TEAM® software was used for data acquisition of EBSD data and the post analysis of the data was carried out in OIM TSL 8 software.

3. Work hardening model

In TRIP HEAs, excellent work hardening is achieved by virtue of deformation-induced γ (f.c.c.) \rightarrow ϵ (h.c.p.) martensitic transformation. Unlike TRIP steels, in which transformation is viable only in the limited retained austenitic volume, larger volume fraction of γ (f.c.c.) austenite is available for transformation in TRIP HEAs; as high as 80% transformation has been reported [7,19]. Fig. 1(a1–a2) and 1 (b1–b2) depict the inverse pole figure and phase map of grains in a Cu-HEA before deformation and after 10% axial strain, respectively, which evidence deformation-induced γ (f.c.c.) \rightarrow ϵ (h.c.p.) martensitic transformation. The microstructure after homogenization at 1100 °C was characterized by 100% γ (f.c.c.) phase. Upon deformation up to 10% axial strain, martensitic transformation was visible where the martensitic volume fraction was determined as 22% from EBSD data (Fig. 1 (b2)). Typical tensile stress-strain response of a TRIP HEA can be divided into three distinct deformation stages (Fig. 1 (c)). Once yield point (σ_0) is reached, stage I hardening is characterized by a rapid decrease in work hardening rate with deformation. Stage II is characterized by a constant work hardening rate, whereas the work hardening rate again decreases at a rapid rate in stage III until the material fractures with minimal post necking extension. Similar work hardening is also observed in other HEAs at cryogenic temperature, in which twinning activity dominates [20]. Stage I is dominated by dislocation-based work hardening mechanisms, whereas γ (f.c.c.) \rightarrow ϵ (h.c.p.) martensitic transformation and deformation twinning are the major strain accommodation mechanisms in Stage II deformation in TRIP/TWIP HEAs [7,20]. Further, deformation-induced martensitic transformation saturates with a resultant reduction in work hardening in Stage III.

An empirical function that replicates such a work hardening behavior ($d\sigma/d\epsilon$) is given by,

$$\frac{d\sigma}{d\epsilon_p} = \beta_0 - \delta \left| \frac{(\epsilon_p - \epsilon_i)}{(\epsilon_i + \epsilon_e)} \right| \tanh^{-1} \left(\frac{\epsilon_p - \epsilon_i}{\epsilon_i + \epsilon_e} \right), \quad \left| \frac{(\epsilon_p - \epsilon_i)}{(\epsilon_i + \epsilon_e)} \right| < 1, \quad (1)$$

where σ is the material flow stress, and ϵ_p is the true plastic strain and ϵ is the equivalent plastic strain. ϵ_p is equal to ϵ under uniaxial loading. Note that the inverse hyperbolic tangent function becomes unbounded at argument values of ± 1 ($\epsilon_p = 0$ and $\epsilon_p = 2\epsilon_i$ in Eqn. (1)), the condition of

Table 1
Alloy composition of as-received Cu-HEA alloy.

At. %	Elements					
	Fe	Mn	Co	Cr	Si	Cu
Nominal (%)	38.5	20	20	15	5	1.5
Actual (%)	38.9 ± 1.1	20.1 ± 1.2	20.4 ± 1.3	14.2 ± 1.2	4.8 ± 1.5	1.6 ± 1.0

which is eliminated by introducing ϵ_e , a very small value of strain in the argument. Specifically, $\epsilon_e = 0.0001$ is used in the present work. Parameter δ controls the rate of reduction in work hardening during Stage I and Stage III. Otherwise, δ controls how abruptly $\frac{d\sigma}{d\epsilon_p} \rightarrow \beta_0$ within $0 \leq \epsilon_p \leq \epsilon_i$. β_0 has the unit of stress and represents the hypothetical constant work hardening rate when $\delta = 0$. Otherwise, β_0 is the value of the work hardening rate at $\epsilon_p = \epsilon_i$, which is the inflection point of the work hardening curve. The function described in Eqn. (1) is continuous, non-negative and bounded in the interval $0 \leq \epsilon_p \leq 2\epsilon_i$.

Integration of Eqn. (1) leads to expression of σ as a function of ϵ_p as follows,

$$\sigma(\epsilon_p) = \beta_0 \epsilon_p \begin{cases} + \left(\delta \frac{(\epsilon_i + \epsilon_e)}{2} \left[(\tanh^{-1} \epsilon^*) (\epsilon^*)^2 + \epsilon^* - \ln \left| \frac{\sqrt{1 + \epsilon^*}}{\sqrt{1 - \epsilon^*}} \right| \right] \right), & (\epsilon_p < \epsilon_i) \\ - \left(\delta \frac{(\epsilon_i + \epsilon_e)}{2} \left[(\tanh^{-1} \epsilon^*) (\epsilon^*)^2 + \epsilon^* - \ln \left| \frac{\sqrt{1 + \epsilon^*}}{\sqrt{1 - \epsilon^*}} \right| \right] \right), & (\epsilon_p \geq \epsilon_i) \end{cases} + C, \quad (2)$$

where $\epsilon^* = \frac{(\epsilon_p - \epsilon_i)}{(\epsilon_i + \epsilon_e)}$ is the argument of the inverse hyperbolic tangent function in Eqn. (1). C is the integration constant, and is determined using the condition $\sigma(0) = \sigma_0$ as follows,

$$C = \sigma_0 - \delta \frac{(\epsilon_i + \epsilon_e)}{2} \left[\tanh^{-1} \left(\frac{(-\epsilon_i)}{(\epsilon_i + \epsilon_e)} \right) \left(\frac{(-\epsilon_i)}{(\epsilon_i + \epsilon_e)} \right)^2 + \frac{(-\epsilon_i)}{(\epsilon_i + \epsilon_e)} - \ln \left| \frac{\sqrt{1 - \frac{(\epsilon_i)}{(\epsilon_i + \epsilon_e)}}}{\sqrt{1 + \frac{(\epsilon_i)}{(\epsilon_i + \epsilon_e)}}} \right| \right]. \quad (3)$$

4. Results

The importance of each model parameter on the work hardening response as well as the true stress-true strain curve is explored. Fig. 2(a) illustrates the change in the work hardening curves for a few arbitrary values of hardening parameters. The arbitrary values used for the model parameters are as follows: $\beta_0 = 2500$, $\epsilon_i = 0.2$, $\epsilon_e = 0.0001$, and $\delta = 1, 10, 100, 500$, and 1000 . Fig. 2(b) shows the true stress-strain response corresponding to the hardening curves in Fig. 2(a). Setting the value of the parameter $\delta = 0$ results in a constant hardening curve, and the stress-strain response is characterized by a linear curve having a yield strength of σ_0 which hardens linearly at the rate β_0 . When metastable TRIP HEAs are considered, such a constant hardening curve idealizes a hypothetical TRIP HEA, which profusely hardens via γ (f.c.c.) \rightarrow ϵ (h.c.p.) martensitic transformation from the onset of yielding to the fracture. With increase in the value of δ , the extent of Stage I and Stage III deformation increases, and the true stress-strain curve replicates typical material flow behavior that is characterized by a reduction in hardening after Stage II, followed by diffuse necking and subsequent failure. Implications of the choice of model parameters for TRIP HEAs and their influence on the tensile stress-strain response have been discussed in the next section.

For TRIP HEAs reported [4–7], post-necking deformation is very minimal, and the material barely necks before failure. Considère's criterion defines the onset of necking as the strain at which the work hardening rate equals flow stress at a specific strain rate,

$$\frac{d\sigma}{d\epsilon}|_{\dot{\epsilon}} = \sigma, \quad (4)$$

where σ is flow stress and ϵ is the equivalent plastic strain. Under uniaxial tensile loading, ϵ is equivalent to the true plastic strain (ϵ_p). Once Considère's criterion is satisfied during uniaxial tensile deformation, the stress-state continuously changes in the necked region which is no more uniaxial. Hence, applying the work hardening model beyond Considère's strain is desired only for problems which involves severe plastic

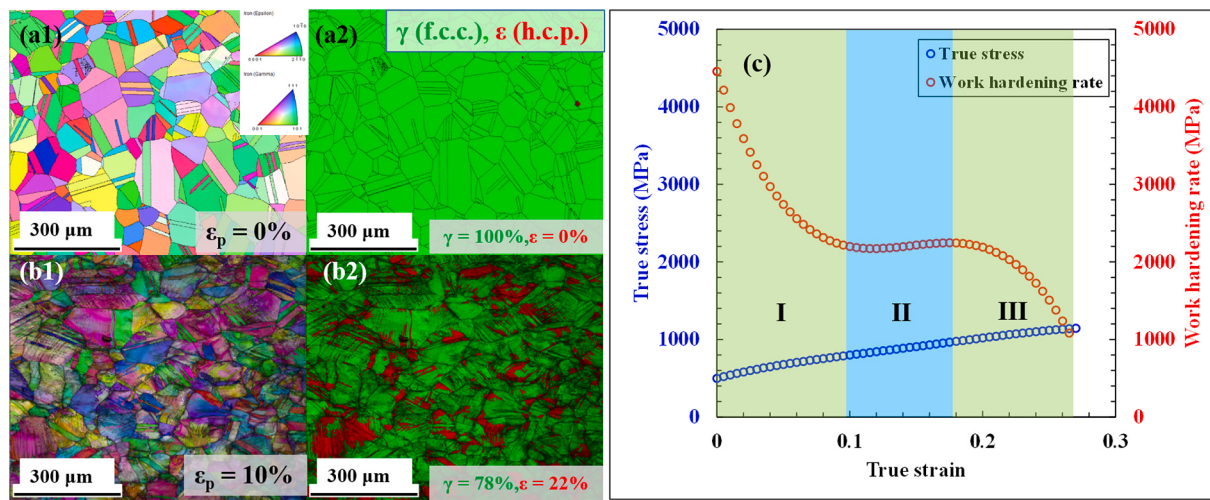


Fig. 1. Microstructure of Cu-HEA indicating γ (f.c.c.) \rightarrow ϵ (h.c.p.) martensitic transformation under uniaxial tensile loading, (a1) IPF map of homogenized alloy and (a2) corresponding phase map, (b1) IPF map and (b2) corresponding phase map after straining to 10%, and (c) true stress-true strain response and work hardening ($d\sigma/d\varepsilon$) behavior of Cu-HEA.

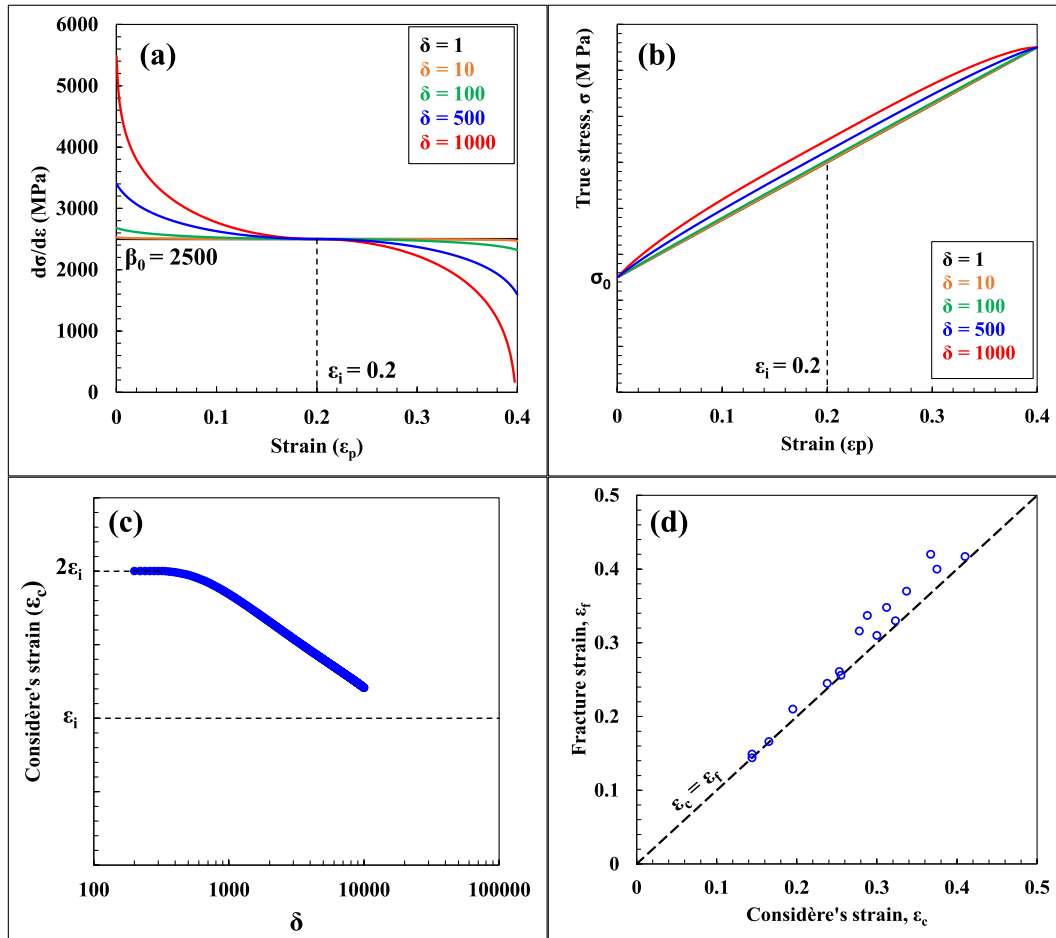


Fig. 2. (a) Graphical representation of work hardening curves according to Eqn. (1) as a function of parameter δ (b) corresponding true stress-true strain curves as per Eqn. 2, (c) variation of Considère's strain as a function of δ , and (d) comparison of fracture strain and Considère's strain for TRIP HEAs reported in literature [4–8, 22]. For graphs (a–c) arbitrary values of σ_0 , β_0 and ε_i are used.

deformation and those demands material failure modeling. While Considère's criterion is based on solid mechanics concepts, Yasnikov et al. [21] have demonstrated that the plastic instability at Considère's strain (ε_c) is dependent on the dislocation evolution; and more importantly, on

the dynamic recovery rate due to cross-slip and dislocation climb. Fig. 2 (c) shows the numerical solution of Eqn. (4) for the present model, in which variation of ε_c with the model parameter δ is plotted. An important observation from Fig. 2(c) is the decrease of ε_c with δ on a semi-log

scale. Additionally, ε_c converges to $2\varepsilon_i$ at very low values of δ ($\delta < 500$) when the work hardening curve approaches the constant hardening curve $\delta = 0$. Otherwise, as the span of the constant hardening stage (stage II) increases (lower values of δ), sustained uniform elongation is achieved and the point of satisfaction of Considère's condition is delayed. For $\delta < 200$, Considère's criterion is not satisfied within the range $0 \leq \varepsilon_p \leq 2\varepsilon_i$; the consequence of which is discussed shortly. As value of δ increases, Considère's condition is satisfied at lower strain levels which implies that necking initiates at an earlier stage of deformation followed by profuse reduction in cross-sectional area at the necking zone, both of which are typical of conventional alloys (see Fig. 3). Fig. 2(a) does show that, as δ decreases, the span of constant hardening in stage II increases. Results from Fig. 2 (a) and 2 (c) when read together suggest that at lower values of δ ($\delta < 1000$), the material undergoes extended uniform elongation and Considère's criterion is satisfied at a larger axial strain value, which is typically the characteristic of metastable TRIP HEAs [4–7]. Table 2 summarizes the Considère's strain, failure strain, and corresponding stress values for various TRIP HEAs reported in literature [4–8,22,23]. A graphical representation of comparison between Considère's strain (ε_c) and fracture strain (ε_f) for various TRIP HEAs is provided in Fig. 2 (d) [4–8,22,23]. A point falling on the dashed line, for which $\varepsilon_f = \varepsilon_c$, confirms an alloy which fails exactly at the Considère's strain. If the alloy undergoes profuse non-uniform deformation associated with necking, the point stays far away from the line $\varepsilon_f = \varepsilon_c$. Closeness of markers in Fig. 2(d), which represents the metastable TRIP HEAs given in Table 2, to the line $\varepsilon_f = \varepsilon_c$ indicates lack of profuse necking and abrupt failure in TRIP HEAs once the Considère's criterion is satisfied; maximum value of $(\varepsilon_f - \varepsilon_c)$ in the tabulated data in Table 2 is ~5.0%.

Fig. 3 (a) shows engineering stress-strain response of conventional alloys SS 304 and INCONEL 625 along with Cu-HEA and $\text{Al}_{0.3}\text{CoCrFeNi}$ TWIP HEA [24]. The plot exhibits extensive necking in SS 304, INCONEL 625 and $\text{Al}_{0.3}\text{CoCrFeNi}$ HEA indicated by significant drop in stress value before failure whereas Cu-HEA fails abruptly; $(\sigma_{UTS} - \sigma_f)$ is equal to 198.5 MPa for SS 304, 172.2 MPa for INCONEL625, 199.9 MPa for $\text{Al}_{0.3}\text{CoCrFeNi}$ HEA whereas for Cu-HEA the value is merely 2.5 MPa. Images of tensile samples obtained after failure also substantiate lack of local necking in Cu-HEA (Fig. 3 (b)–(e)). Measurement of dimensions at the neck and outside the neck after failure, which signifies the extent of non-uniform elongation and necking once Considère's condition is satisfied, revealed substantial area reduction of 62.3% and 36.1% in SS 304 and INCONEL 625, respectively, whereas the area reduction is only 9.3% in Cu-HEA.

5. Discussion

5.1. Determination of model parameters

For TRIP HEAs reported, model parameters were identified by curve fitting the true stress-strain curves. First, σ_0 was identified from the literature for individual HEAs. Next, ε_i was determined by identifying the fracture strain; typically ε_i is approximately half of the fracture strain for TRIP HEAs [4–7]. Subsequently, β_0 was identified by matching the linear Stage II hardening stress; and, finally, δ was identified by matching the curvature of the stress-strain response in Stage I and Stage III by minimizing the least-squares error between the experimental and model true stress-true strain curves. Further error optimization was achieved by refining the values of ε_i and δ . Fig. 4(a–c) show the representative model fitting for two TRIP HEAs [5,7] and CoCrFeMnNi HEA [20], and indicate excellent matching with experimental results. Optimized model parameters for other TRIP HEAs and several medium and high Mn TRIP/TWIP steels reported in literature with similar work hardening response are provided in Table 3. For completeness, corresponding comparison of experimental and model fits is given as supplementary data Fig. S1.

Lloyd et al. [18] have used hyperbolic tangent function to describe the hardening curve for TRIP and TWIP steels and suggested that the function retains non-zero value even at large values of strain, which is beneficial for implicit numerical implementation. They neglected narrow Stage I hardening in their model by assuming that its contribution to material toughness is negligible. However, in TRIP HEAs, Stage I deformation is appreciable due to early TRIP activity (Fig. 1(c)) and hence cannot be neglected. Fig. 5 compares the work hardening rate and corresponding true stress-strain response for a TRIP HEA reported in literature [5] according to the current model and model proposed by Lloyd et al. [18]. Parameters used for the model fits are provided in the inset of Fig. 3 following the notations used in [18] as well as Eqns. (1) and (2). Note the present model's potential to include the work hardening response during stage I of deformation which is considered negligible in Ref. [18]. Also, the better fit obtained for true stress-strain response for the present model compared to the model proposed in Ref. [18] justifies the necessity of considering the stage I deformation in TRIP HEAs, which otherwise resulted in 6% reduction in material toughness.

The hardening function described in Eqn. (1) is defined over the range $0 \leq \varepsilon_p \leq 2\varepsilon_i$. Beyond $2\varepsilon_i$, the function becomes unbounded. Hence, for materials exhibiting severe necking, where failure occurs at strain levels beyond $2\varepsilon_i$, the model is insufficient to accommodate such extensive non-uniform elongation till failure (where the equivalent

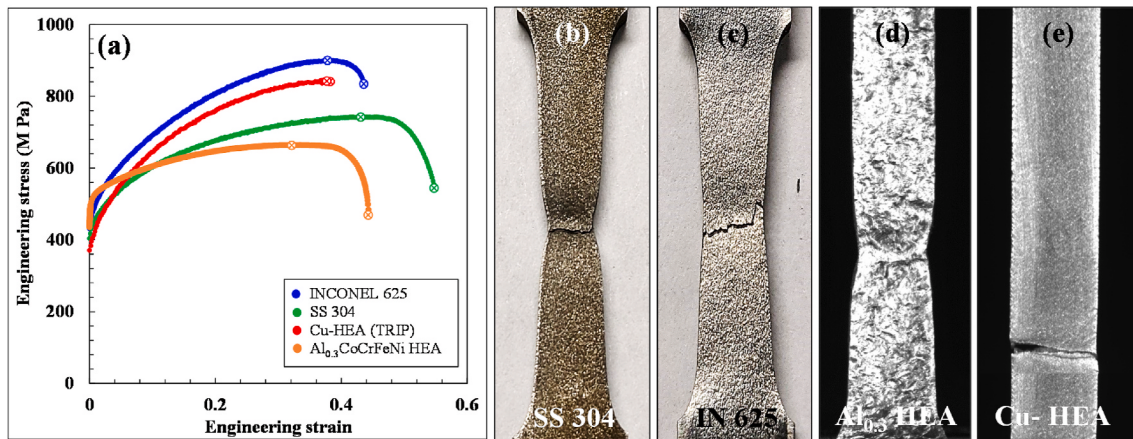


Fig. 3. (a) Engineering stress-strain response of HEAs and conventional alloys and images of tensile specimens after failure under uniaxial tension indicating severe necking in (b) SS 304, (c) INCONEL 625, (d) $\text{Al}_{0.3}\text{CoCrFeNi}$ HEA, and lack of necking in (e) Cu-TRIP HEA. (Markers with a cross in (a) indicate strains corresponding to UTS and fracture.)

Table 2

Considère's strain, fracture strain, true stress corresponding to Considère's strain, failure stress, and the difference between Considère's strain and failure strains for metastable TRIP HEAs reported in literature.

TRIP HEA	ε_c	ε_f	σ_c	σ_f	$\varepsilon_f - \varepsilon_c$	Condition	Reference
Fe _{38.5} Mn ₂₀ Co ₂₀ Cr ₁₅ Si ₅ Cu _{1.5}	0.29	0.33	1391	1428	0.04	FSP	[7]
	0.31	0.35	1396	1433	0.04	FSP	[7]
	0.29	0.34	1456	1540	0.01	FSP	[7]
	0.17	0.17	1530	1534	0.00	AM	[23]
	0.15	0.15	1385	1392	0.00	AM	[23]
Fe ₄₀ Mn ₂₀ Co ₂₀ Cr ₁₅ Si ₅	0.35	0.36	1053	1050	0.01	HT	*
	0.20	0.21	1235	1246	0.02	FSP	[6]
	0.24	0.25	1423	1433	0.01	FSP	[6]
	0.14	0.15	771	771	0.01	AM	[22]
	0.25	0.26	1396	1414	0.01	AM	[22]
Fe ₃₉ Mn ₂₀ Co ₂₀ Cr ₁₅ Si ₅ Al ₁	0.32	0.33	1570	1578	0.01	FSP	[6]
	0.37	0.42	1419	1468	0.05	FSP + HT	[5]
	0.34	0.37	1457	1488	0.03	FSP + HT	[5]
Fe ₅₀ Mn ₃₀ Co ₁₀ Cr ₁₀	0.26	0.26	1368	1371	0.00	FSP + HT	[5]
	0.36	0.41	883	888	0.05	HT	[4]
	0.33	0.35	1194	1182	0.02	FSP	[4]
	0.40	0.43	1312	1301	0.03	FSP	[4]

FSP: Friction stir processed; AM: Additively manufactured; HT: Heat treated; *: Current study.

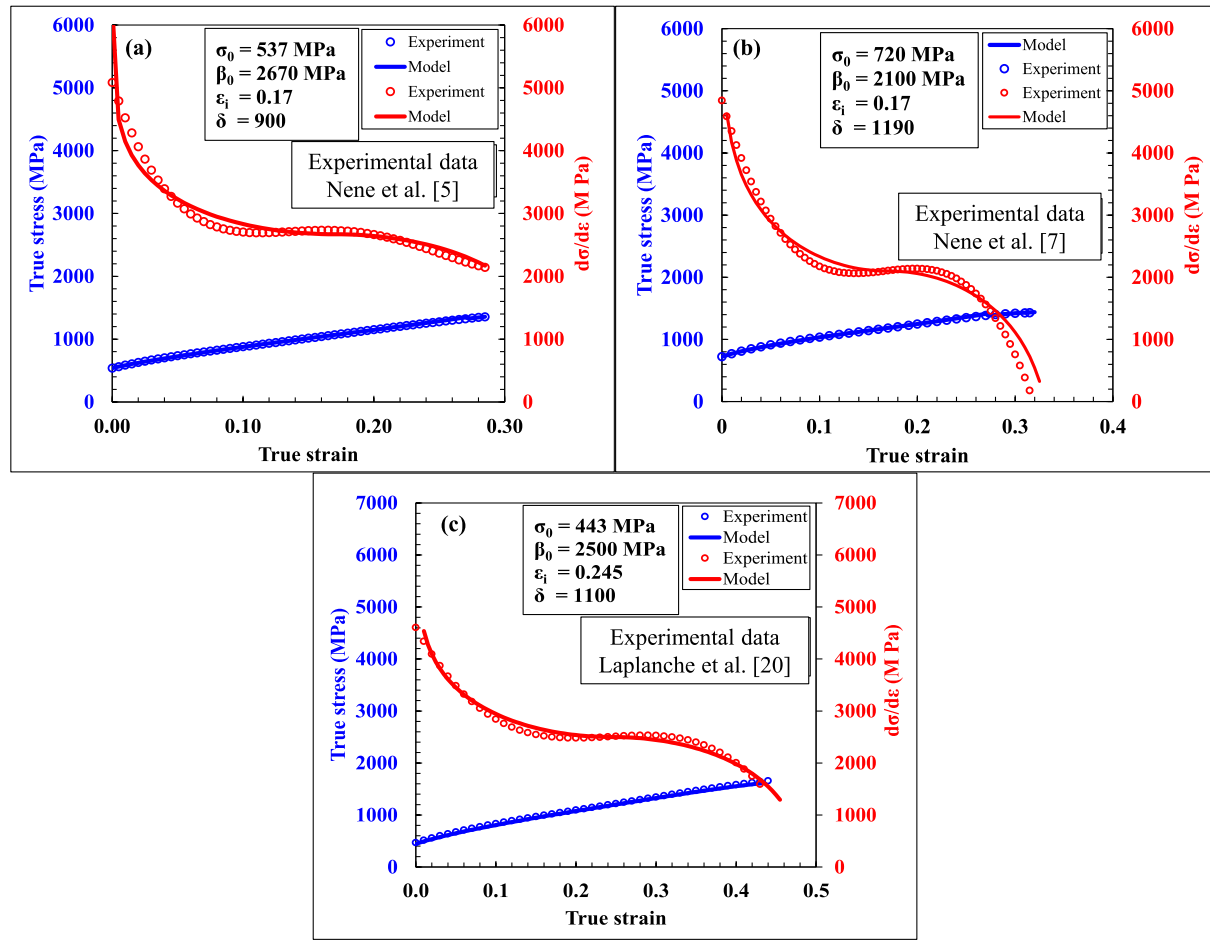


Fig. 4. Comparison of the model fits with experimental results, (a) Fe₃₉Mn₂₀Co₂₀Cr₁₅Si₅Al₁ HEA [5], (b) Fe_{38.5}Mn₂₀Co₂₀Cr₁₅Si₅Cu_{1.5} HEA [7], and (c) CoCrFeMnNi HEA [20].

plastic strain in the necked region is considerably higher than the nominal strain [18]). However, the model is still capable to predict the mechanical response in the uniform elongation stage up to necking at which the Considère's criterion is satisfied. Also, as mentioned in section 4, values of $\delta < 200$ does not provide a solution to Considère's criterion. At such low values of δ , the extended stage II hardening denied the solution to Eqn. (4) in the valid strain range of the model, $0 \leq \varepsilon_p \leq 2\varepsilon_b$

within which Eqns. (1) and (2) are bounded. In order to check the applicability of the model to metastable TRIP HEAs, one has to confirm the existence of Considère's strain and preferably the failure strain within the range $0 \leq \varepsilon_p \leq 2\varepsilon_b$. A comparison of ε_i , ε_c , and ε_f for all TRIP HEAs indicates that Considère's strain is below $2\varepsilon_b$, the upper bound of the model (Table 3). Additionally, in TRIP HEAs for which failure occurs abruptly without severe necking, strain at failure in the necked region is

Table 3

SFE and best fit model parameters of Eqn. (1) and Eqn. (2) for various TRIP HEAs as well as medium and high Mn steels reported in literature.

SFE [mJ mol ⁻¹]	β_0 [MPa]	ε_i	δ	σ_0 [MPa]	ε_c	ε_f	Ref.
13.1	2100	0.17	1190	720	0.31	0.35	[7], ^a
13.2	2200	0.165	1000	809	0.29	0.34	[7]
15.2	2670	0.17	900	537	0.32	0.36	[5], ^a
15.3	2800	0.145	850	635	0.26	0.29	[5]
15.4	2400	0.21	860	500	0.37	0.42	[5]
15.2	2320	0.175	1100	610	0.34	0.37	[5]
15.4	2510	0.195	1120	655	0.36	0.40	[5]
15.4	2650	0.165	1010	675	0.31	0.34	[5]
7.1	2830	0.163	950	650	0.32	0.33	[6]
7.75	2500	0.245	1100	443	0.43	0.64	[20], ^a
13.2	1950	0.21	1050	385	0.36	0.41	[4]
13.6	3200	0.175	1140	251	0.33	0.35	[4]
-2.1	12500	0.075	10500	210	0.12	0.18	[18, 25]
0.7	7100	0.11	8300	240	0.16	0.23	[18, 25]
8.9	3050	0.23	400	400	0.42	0.48	[18, 25]
19.9	2990	0.17	500	400	—	—	[18, 25]
8.1	2850	0.12	600	355	0.23	0.25	[18, 25]
19.0	2450	0.26	490	240	0.53	0.54	[9]
10.0	3600	0.18	400	540	0.35	0.36	[9]
45.8	1520	0.275	350	275	0.53	0.54	[27]
-0.7	5200	0.175	480	221	0.33	0.36	[18, 28]
-1.9	6300	0.14	520	170	0.25	0.26	[18, 28]
9.5	2600	0.27	570	508	0.41	0.45	[18, 28]
10.6	2540	0.285	450	325	0.52	0.58	[18, 29]
24.0	2050	0.27	500	345	0.53	0.60	[18, 29]
29.6	2070	0.265	500	370	0.48	0.53	[18, 29]
33.6	1980	0.25	460	400	0.52	0.59	[18, 29]

^a Model fits illustrated in Fig. 4.

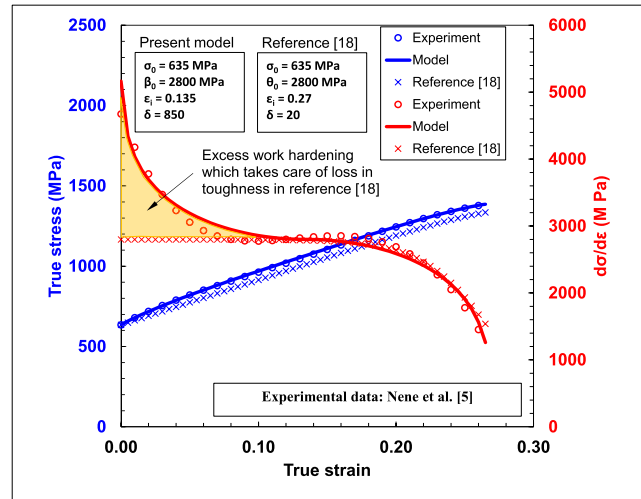


Fig. 5. Comparison of the fits obtained for work hardening response and true stress-strain curve according to Ref. [18] and the present model for a TRIP HEA reported in [5]. Y-axis scales are adjusted on both left and right axes for better resolution.

$\sim 2\varepsilon_b$, which confirms the applicability of the presented model to describe the entire stress-strain response (Fig. 2 (d)). Strain levels below $2\varepsilon_i$ also ensure that the hardening curve remains non-negative during deformation, which facilitates numerical implementation of the model.

5.2. Determination of SFE

To determine SFE and to correlate with the model parameters, we use the description for energy to form a stacking fault formulated by Olson and Cohen [30].

$$SFE = np(\Delta G_{chem}^{\gamma \rightarrow \epsilon} + E^{str}) + 2\sigma^{\gamma/\epsilon}, \quad (5)$$

where, per Olson and Cohen, $n = 2$ is the number of faulted planes that act as martensitic nuclei, ρ is the planar atomic density of the f.c.c. close packed {1 1 1} planes, which is determined as 2.97×10^{-5} mol m⁻² using the value of lattice parameter $a_{f.c.c.} = 3.5912$ Å [31]; $\Delta G_{chem}^{\gamma \rightarrow \epsilon}$ is the chemical driving force for austenite-martensite transformation; $E^{str} = 22.2$ J/mol is energy barrier for transformation [32]; and $\sigma^{\gamma/\epsilon} = 15$ mJ/mol is the interfacial energy between the two phases [32]. The values of $\Delta G_{chem}^{\gamma \rightarrow \epsilon}$ for different TRIP HEAs were reported in [32,33]. Lloyd et al. [18] have demonstrated determination of SFE as a function of alloy composition and shown the compositional dependence on their model parameters as a function of SFE. Further, extrinsic dependence of grain size on stacking fault generation ($\Delta G_{ex}^{\gamma \rightarrow \epsilon}$) is considered, and is described as [34],

$$\Delta G_{ex}^{\gamma \rightarrow \epsilon} = k_1 \exp(-d/k_2), \quad (6)$$

where d is austenitic grain size, k_1 (170.06 J/mol) and k_2 (18.55 μm) were determined experimentally for TRIP steels [34]. Hence, Eqn. (5) is modified to obtain the effective SFE as:

$$SFE = np(\Delta G_{chem}^{\gamma \rightarrow \epsilon} + E^{str} + \Delta G_{ex}^{\gamma \rightarrow \epsilon}) + 2\sigma^{\gamma/\epsilon}. \quad (7)$$

For illustration, SFE for CS-TRIP HEA [35] was determined experimentally as 6.31 mJ m⁻² using neutron diffraction and the value obtained using Eqn. (7) is 7.19 mJ m⁻², closeness of which confirms the applicability of the aforementioned equations to determine SFE. Effective SFE for TRIP/TWIP HEAs [4–8,20] as well as certain medium and high Mn TRIP/TWIP steels [9,18,25–29,36] having similar work hardening response are tabulated in Table 3. Fig. 6 (a)–(d) is the graphical representation of Table 3 in which the model parameters are correlated with SFE. Regression fits indicate that parameters β_0 and ε_i fit well to a power and linear law, respectively. As mentioned before, parameter β_0 defines the constant Stage II hardening, which depends on deformation and transformation mechanisms as well as intrinsic resistance to plastic flow. Similarly, parameter ε_i dictates the final stage of hardening where the transformed volume reaches its peak and the grains become saturated with dislocations and ceases its evolution, thereby leading to abrupt failure. Further, the aforementioned micro-mechanisms depend strongly on effective SFE of the alloy and hence justify the trends in Fig. 6 (a) and 6 (c). As shown in Fig. 2 (a), parameter δ controls the rate of drop in work hardening in Stages I and III. Higher value of δ for TRIP HEAs compared to TRIP and TWIP steels (Fig. 6 (d)) indicates onset of martensitic transformation during early deformation stage unlike TRIP steels, for which transformation is limited and delayed to a later stage. Although δ lacks a trend with SFE, a value of $\delta = 1040$ and 500 fits reasonably for all TRIP HEAs and TRIP/TWIP steels, respectively. A higher value of δ for TRIP HEAs compared to TRIP steels indicates that the Considère's condition for TRIP HEAs is satisfied at slightly lower value than TRIP steel (see Fig. 2 (c)). Fig. 7 (a) shows a schematic of work hardening rate curve and true stress-strain curve for TRIP steels, TRIP HEAs, and conventional alloys. Note that with increase in value of δ , the Considère's condition is satisfied at a lower strain level. Closeness of Considère's strain for TRIP HEAs and TRIP steels to $2\varepsilon_i$, the upper bound of the work hardening function, demonstrates the applicability of

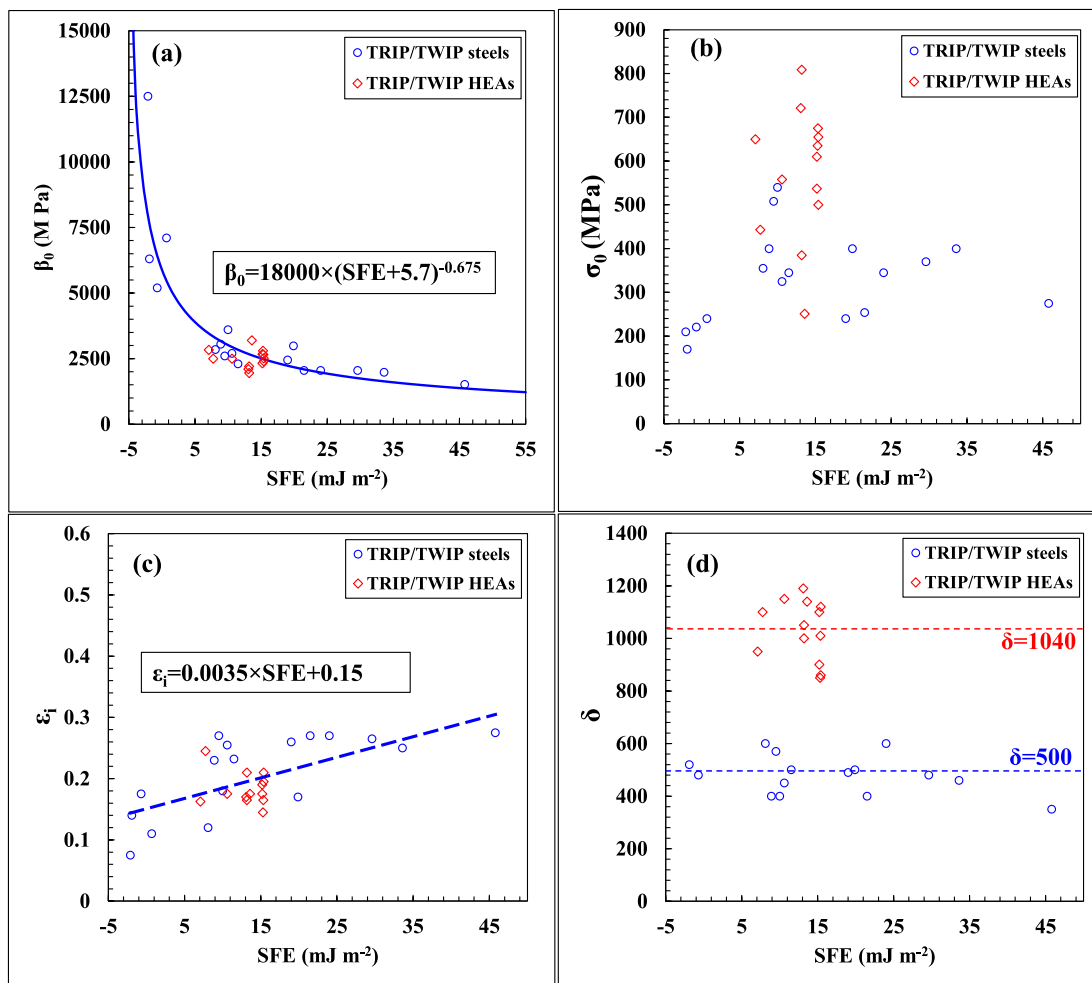


Fig. 6. Variation of model parameters as a function of SFE obtained for TRIP HEAs [4–8,22] and TRIP/TWIP steels [9,20,25–29], (a) β_0 , (b) ε_i , (c) σ_0 , and (d) δ .

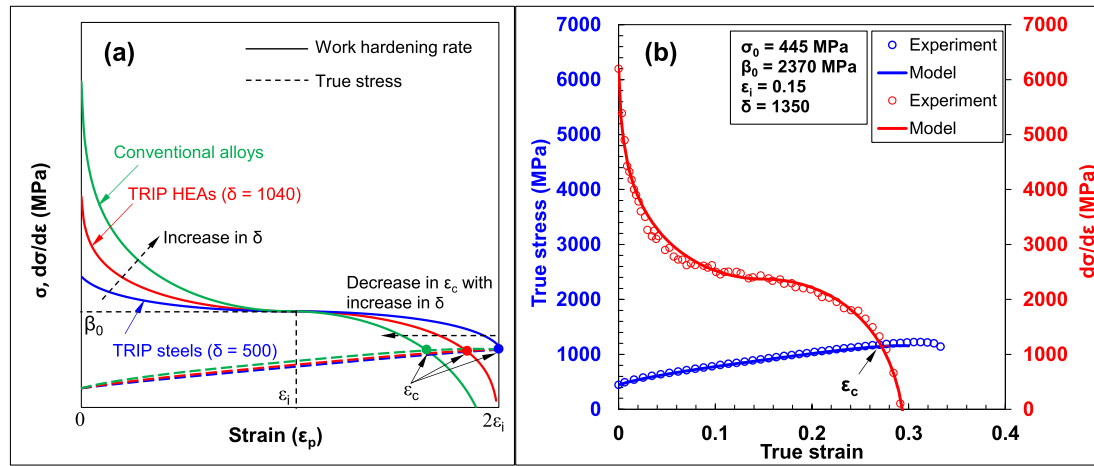


Fig. 7. (a) Schematic showing the variation in work hardening curve with increase in the value of model parameter δ for TRIP HEA, TRIP steel, and conventional alloy. Note that Considère's condition is satisfied at lower strain value for conventional alloys at higher values of δ , and (b) model fit for INCONEL 625.

the model to describe almost the entire stress-strain response for those alloys when compared to conventional alloys for which the Considère's condition is satisfied at a comparatively lower strain level. Fig. 7 (b) shows the model fit for INCONEL 625 along with the value of model parameters. Model fitted well for relatively higher value of $\delta = 1350$ compared to TRIP HEAs ($\delta = 1040$) and TRIP steels ($\delta = 500$). Note that

Considère's condition is satisfied at a rather low strain value of $\varepsilon_p = 0.27$ compared to $\varepsilon_f = 0.34$. Additionally, the model is not able to capture the entire stress-strain response of the alloy due to severe necking and extended failure. Parameter σ_0 indicated the least trend with SFE (Fig. 6 (b)) since yield strength is greatly influenced by grain size [8], processing route [5,37], secondary phases [37], and initial phase fraction

[4].

5.3. Model validation

Model validity by means of parametric dependence on SFE and microstructure was established using experimental results of two TRIP HEA compositions that were not used to obtain the regression fits in Fig. 6 (a)–(d) [5,7]. As mentioned in section 5.2, σ_0 did not correlate well with SFE. Hence we used the Hall-Petch relationship obtained for Cu-HEA in [7],

$$\sigma_0 = \sigma_k + \frac{k_y}{\sqrt{d}}, \quad (8)$$

where $\sigma_k = 470$ MPa and $k_y = 271$ MPa $\sqrt{\text{m}}$. The grain size reported for Cu-HEA in the FSP condition S350 is $6.57 \mu\text{m}$ [7], which when substituted in Eqn. (8) gives the value of $\sigma_0 = 575$ MPa. The parameter δ also lacked a definite correlation with SFE; however, as mentioned in section 5.2, $\delta = 1040$ gives a reasonable fit to all TRIP HEAs. Using Eqn. (7), SFE of 10.6 mJ m^{-2} was used in the respective regression fit equations for β_0 and ε_i . A similar procedure was also used for $\text{Fe}_{39}\text{Mn}_{20}\text{Co}_{20}\text{Cr}_{15}\text{Si}_5\text{Al}_1$ TRIP HEA [5]. The grain size reported for the alloy was $0.8 \mu\text{m}$, for which SFE was 15.3 mJ m^{-2} . Although Nene et al. [5] did not report the Hall-Petch strengthening coefficients for $\text{Fe}_{39}\text{Mn}_{20}\text{Co}_{20}\text{Cr}_{15}\text{Si}_5\text{Al}_1$ TRIP HEA, a value of $\sigma_0 = 680$ MPa fitted well for all the microstructures reported, and hence was used for validation. Fig. 8 validates the model as a function of SFE and initial microstructure using the trends obtained in Fig. 6 (a)–(d), and the good fit justifies the applicability of model as a predictive tool to obtain the tensile response of metastable TRIP HEAs as a function of SFE.

6. Conclusions

Metastable high entropy alloys undergoes γ (f.c.c) to ϵ (h.c.p) martensitic transformation under deformation. The work hardening response of a metastable TRIP HEA is characterized by an initial stage of

drop in hardening rate with deformation dominated by dislocation activity, second stage of constant work hardening rate characterized by profuse γ (f.c.c) to ϵ (h.c.p) martensitic transformation, and a final stage of drop in hardening rate which subsequently lead to failure. Unlike conventional alloys which fails after severe necking, failure of TRIP HEAs is characterized by lack of profuse necking and abrupt failure close to UTS. A four-parameter hardening model was developed based on the nature of work hardening curve for TRIP/TWIP HEAs as well as TRIP/TWIP steels. The model parameters identified for the alloys correlated well with their respective effective SFE. Reasonably good fit was obtained using the parametrical trend with SFE, which confirmed the applicability of the model as a predictive tool to obtain tensile stress-strain response from SFE.

Data availability statement

The raw/processed data required to reproduce these findings cannot be shared at this time as the data also forms part of an ongoing study.

CRediT authorship contribution statement

Ravi Sankar Haridas: Conceptualization, Data curation, Formal analysis, Methodology, Writing – original draft. **Priyanshi Agrawal:** Methodology, Formal analysis, Writing – review & editing. **Rajiv S. Mishra:** Conceptualization, Project administration, Resources, Supervision, Writing – review & editing.

Declaration of competing interest

The authors declare that they have no known competing financial interests or personal relationships that could have appeared to influence the work reported in this paper.

Acknowledgments

The present work was performed under the cooperative agreement between the Army Research Laboratory (ARL) and the University of North Texas (W911NF-18-2-0067). Authors acknowledge Materials Research Facility at University of North Texas for access to scanning electron microscopy. Authors are also grateful to Dr. Jeffrey T. Lloyd for his valuable suggestions.

Appendix A. Supplementary data

Supplementary data to this article can be found online at <https://doi.org/10.1016/j.msea.2021.141778>.

References

- [1] J.W. Yeh, S.K. Chen, S.J. Lin, J.Y. Gan, T.S. Chin, T.T. Shun, C.H. Tsau, S.Y. Chang, Nanostructured high-entropy alloys with multiple principal elements: novel alloy design concepts and outcomes, *Adv. Eng. Mater.* 6 (2004) 299–303, <https://doi.org/10.1002/adem.200300567>.
- [2] Y. Zhang, T. Ting, Z. Tang, M.C. Gao, K.A. Dahmen, P.K. Liaw, Z. Ping, Progress in materials science microstructures and properties of high-entropy alloys, *J. Prog. Mater. Sci.* 61 (2014) 1–93, <https://doi.org/10.1016/j.jpmatsci.2013.10.001>.
- [3] Z. Li, K.G. Pradeep, Y. Deng, D. Raabe, C.C. Tasan, Metastable high-entropy dual-phase alloys overcome the strength–ductility trade-off, *Nature* 534 (2016) 227–230, <https://doi.org/10.1038/nature17981>.
- [4] S.S. Nene, K. Liu, M. Frank, R.S. Mishra, R.E. Brennan, K.C. Cho, Z. Li, D. Raabe, Enhanced strength and ductility in a friction stir processing engineered dual phase high entropy alloy, *Sci. Rep.* 7 (2017) 16167, <https://doi.org/10.1038/s41598-017-16509-9>.
- [5] S.S. Nene, S. Sinha, M. Frank, K. Liu, R.S. Mishra, B.A. McWilliams, K.C. Cho, Unexpected strength–ductility response in an annealed, metastable, high-entropy alloy, *Appl. Mater. Today* 13 (2018) 198–206, <https://doi.org/10.1016/J.AMPT.2018.09.002>.
- [6] S.S. Nene, M. Frank, K. Liu, S. Sinha, R.S. Mishra, B. McWilliams, K.C. Cho, Reversed strength–ductility relationship in microstructurally flexible high entropy alloy, *Scripta Mater.* 154 (2018) 163–167, <https://doi.org/10.1016/J.SCRIPTAMAT.2018.05.043>.

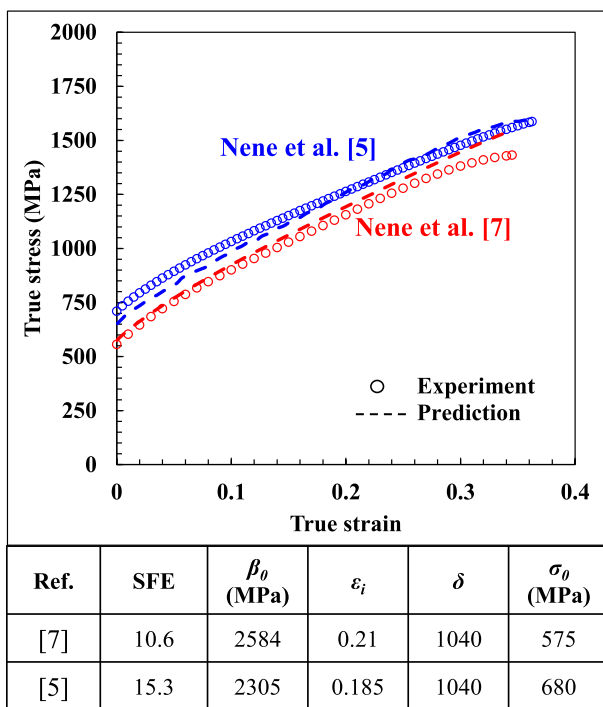


Fig. 8. Illustration of model prediction using the correlated parameters as a function of SFE with experiments [5,7] along with the value of parameters used for prediction.

- [7] S.S. Nene, M. Frank, K. Liu, S. Sinha, R.S. Mishra, B.A. McWilliams, K.C. Cho, Corrosion-resistant high entropy alloy with high strength and ductility, *Scripta Mater.* 166 (2019) 168–172, <https://doi.org/10.1016/J.SCRIPTAMAT.2019.03.028>.
- [8] S.S. Nene, M. Frank, K. Liu, R.S. Mishra, B.A. McWilliams, K.C. Cho, Extremely high strength and work hardening ability in a metastable high entropy alloy, *Sci. Rep.* 8 (2018) 9920, <https://doi.org/10.1038/s41598-018-28383-0>.
- [9] S. Allain, J.P. Chateau, O. Bouaziz, S. Migot, N. Guelton, Correlations between the calculated stacking fault energy and the plasticity mechanisms in Fe-Mn-C alloys, *Mater. Sci. Eng.* (2004) 387–389, <https://doi.org/10.1016/j.msea.2004.01.059>, 158–162.
- [10] S. Kibey, J.B. Liu, D.D. Johnson, H. Sehitoglu, Predicting twinning stress in fcc metals: linking twin-energy pathways to twin nucleation, *Acta Mater.* 55 (2007) 6843–6851, <https://doi.org/10.1016/j.actamat.2007.08.042>.
- [11] R.S. Mishra, R.S. Haridas, P. Agrawal, High entropy alloys – tunability of deformation mechanisms through integration of compositional and microstructural domains, *Mater. Sci. Eng.* 812 (2021) 141085, <https://doi.org/10.1016/j.msea.2021.141085>.
- [12] A. Arsenlis, D.M. Parks, Crystallographic aspects of geometrically-necessary and statistically-stored dislocation density, *Acta Mater.* 47 (1999) 1597–1611, [https://doi.org/10.1016/S1359-6454\(99\)00020-8](https://doi.org/10.1016/S1359-6454(99)00020-8).
- [13] Y. Estrin, L.S. Tóth, A. Molinari, Y. Bréchet, A dislocation-based model for all hardening stages in large strain deformation, *Acta Mater.* 46 (1998) 5509–5522, [https://doi.org/10.1016/S1359-6454\(98\)00196-7](https://doi.org/10.1016/S1359-6454(98)00196-7).
- [14] E.I. Galindo-Navia, P.E.J. Rivera-Díaz-del-Castillo, Understanding martensite and twin formation in austenitic steels: a model describing TRIP and TWIP effects, *Acta Mater.* 128 (2017) 120–134, <https://doi.org/10.1016/j.actamat.2017.02.004>.
- [15] O. Bouaziz, J. Moon, H.S. Kim, Y. Estrin, Isotropic and kinematic hardening of a high entropy alloy, *Scripta Mater.* 191 (2021) 107–110, <https://doi.org/10.1016/j.scriptamat.2020.09.022>.
- [16] R.G. Stringfellow, D.M. Parks, G.B. Olson, A constitutive model for transformation plasticity accompanying strain-induced martensitic transformations in metastable austenitic steels, *Acta Metall. Mater.* 40 (1992) 1703–1716, [https://doi.org/10.1016/0956-7151\(92\)90114-T](https://doi.org/10.1016/0956-7151(92)90114-T).
- [17] I. Papantoniadis, M. Agoras, N. Aravas, G. Haidemenopoulos, Constitutive modeling and finite element methods for TRIP steels, *Comput. Methods Appl. Mech. Eng.* 195 (2006) 5094–5114, <https://doi.org/10.1016/j.cma.2005.09.026>.
- [18] J.T. Lloyd, D.M. Field, K.R. Limmer, A four parameter hardening model for TWIP and TRIP steels, *Mater. Des.* 194 (2020), <https://doi.org/10.1016/j.matdes.2020.108878>.
- [19] R.S. Haridas, P. Agrawal, S. Thapliyal, S. Yadav, Strain rate sensitive microstructural evolution in a TRIP assisted high entropy alloy: experiments, microstructure and modeling, *Mech. Mater.* 156 (2021) 103798, <https://doi.org/10.1016/j.mechmat.2021.103798>.
- [20] G. Laplanche, A. Kostka, O.M. Horst, G. Eggeler, E.P. George, Microstructure evolution and critical stress for twinning in the CrMnFeCoNi high-entropy alloy, *Acta Mater.* 118 (2016) 152–163, <https://doi.org/10.1016/j.actamat.2016.07.038>.
- [21] I.S. Yasinikov, A. Vinogradov, Y. Estrin, Revisiting the Considère criterion from the viewpoint of dislocation theory fundamentals, *Scripta Mater.* 76 (2014) 37–40, <https://doi.org/10.1016/j.scriptamat.2013.12.009>.
- [22] P. Agrawal, S. Thapliyal, S.S. Nene, R.S. Mishra, B.A. McWilliams, K.C. Cho, Excellent strength-ductility synergy in metastable high entropy alloy by laser powder bed additive manufacturing, *Addit. Manuf.* 32 (2020) 101098, <https://doi.org/10.1016/J.ADDMA.2020.101098>.
- [23] S. Thapliyal, S.S. Nene, P. Agrawal, T. Wang, C. Morphew, R.S. Mishra, B.A. McWilliams, K.C. Cho, Damage-tolerant, corrosion-resistant high entropy alloy with high strength and ductility by laser powder bed fusion additive manufacturing, *Addit. Manuf.* 36 (2020) 101455, <https://doi.org/10.1016/j.addma.2020.101455>.
- [24] Z. Li, S. Zhao, H. Diao, P.K. Liaw, M.A. Meyers, High-velocity deformation of Al0.3CoCrFeNi high-entropy alloy: remarkable resistance to shear failure, *Sci. Rep.* 7 (2017) 42742, <https://doi.org/10.1038/srep42742>.
- [25] D.M. Field, J. Qing, D.C. Van Aken, Chemistry and properties of medium-Mn two-stage TRIP steels, *Metall. Mater. Trans. A Phys. Metall. Mater. Sci.* 49 (2018) 4615–4632, <https://doi.org/10.1007/s11661-018-4798-6>.
- [26] B.C. De Cooman, O. Kwon, K.G. Chin, State-of-the-knowledge on TWIP steel, *Mater. Sci. Technol.* 28 (2012) 513–527, <https://doi.org/10.1179/1743284711Y.0000000095>.
- [27] F.X. Yin, H. Xia, J.H. Feng, M.H. Cai, X. Zhang, G.K. Wang, T. Sawaguchi, Mechanical properties of an Fe-30Mn-4Si-2Al alloy after rolling at different temperatures ranging from 298 to 1073 K, *Mater. Sci. Eng.* 725 (2018) 127–137, <https://doi.org/10.1016/j.msea.2018.03.079>.
- [28] M.F. Buchely, D.M. Field, D.C. Van Aken, Analysis of hot- and cold-rolled loads in medium-Mn TRIP steels, *Metall. Mater. Trans. B Process Metall. Mater. Process. Sci.* 50 (2019) 1180–1192, <https://doi.org/10.1007/s11663-019-01566-4>.
- [29] J.K. Hwang, Revealing the small post-necking elongation in twinning-induced plasticity steels, *J. Mater. Sci.* 55 (2020) 8285–8302, <https://doi.org/10.1007/s10853-020-04477-x>.
- [30] G.B. Olson, M. Cohen, A general mechanism of martensitic nucleation: Part I. General concepts and the FCC → HCP transformation, *Metall. Trans. A* 7 (1976) 1897–1904, <https://doi.org/10.1007/BF02659822>.
- [31] S. Sinha, S.S. Nene, M. Frank, K. Liu, P. Agrawal, R.S. Mishra, On the evolving nature of c/a ratio in a hexagonal close-packed epsilon martensite phase in transformative high entropy alloys, *Sci. Rep.* 9 (2019) 1–14, <https://doi.org/10.1038/s41598-019-49904-5>.
- [32] W. Lu, C.H. Liebscher, G. Dehm, D. Raabe, Z. Li, Bidirectional transformation enables hierarchical nanolaminate dual-phase high-entropy alloys, *Adv. Mater.* 30 (2018) 1–10, <https://doi.org/10.1002/adma.201804727>.
- [33] S.S. Nene, M. Frank, P. Agrawal, S. Sinha, K. Liu, S. Shukla, R.S. Mishra, B.A. McWilliams, K.C. Cho, Microstructurally flexible high entropy alloys: linkages between alloy design and deformation behavior, *Mater. Des.* 194 (2020) 108968, <https://doi.org/10.1016/j.matdes.2020.108968>.
- [34] O.A. Zambrano, Stacking fault energy maps of Fe-Mn-Al-C-Si steels: effect of temperature, grain size, and variations in compositions, *J. Eng. Mater. Technol. Trans. ASME.* 138 (2016) 1–9, <https://doi.org/10.1115/1.4033632>.
- [35] M. Frank, Y. Chen, S.S. Nene, S. Sinha, K. Liu, K. An, R.S. Mishra, Investigating the deformation mechanisms of a highly metastable high entropy alloy using in-situ neutron diffraction, *Mater. Today Commun.* 23 (2020) 100858, <https://doi.org/10.1016/J.MTCOMM.2019.100858>.
- [36] D.M. Field, D.C. Van Aken, Dynamic strain aging phenomena and tensile response of medium-Mn TRIP steel, *Metall. Mater. Trans. A Phys. Metall. Mater. Sci.* 49 (2018) 1152–1166, <https://doi.org/10.1007/s11661-018-4481-y>.
- [37] B. Gwalani, S. Gorsse, D. Choudhuri, M. Styles, Y. Zheng, R.S. Mishra, R. Banerjee, Modifying transformation pathways in high entropy alloys or complex concentrated alloys via thermo-mechanical processing, *Acta Mater.* 153 (2018) 169–185, <https://doi.org/10.1016/j.actamat.2018.05.009>.